RESEARCH ARTICLE | SEPTEMBER 22 2023

Analysis of an innovative compact point absorber wave energy converter concept suitable for small-scale power applications *⊙*

Special Collection: Recent Advances in Marine Hydrodynamics

Vishnu Vijayasankar ⊚ ; Suman Kumar; Abdus Samad 🗷 ⊚ ; Lei Zuo 🗷 ⊚



Physics of Fluids 35, 097140 (2023)

https://doi.org/10.1063/5.0165877

A CHORUS









Analysis of an innovative compact point absorber wave energy converter concept suitable for small-scale power applications

Cite as: Phys. Fluids 35, 097140 (2023); doi: 10.1063/5.0165877 Submitted: 30 June 2023 · Accepted: 27 August 2023 · Published Online: 22 September 2023









Vishnu Vijayasankar,^{1,a)} (i) Suman Kumar,^{2,b)} Abdus Samad,^{2,c)} (ii) and Lei Zuo^{1,c)} (iii)





AFFILIATIONS

Naval Architecture and Marine Engineering, University of Michigan, Ann Arbor, Michigan 48109, USA

Note: This paper is part of the special topic, Recent Advances in Marine Hydrodynamics.

ABSTRACT

In response to the need for efficient, small-scale power sources for applications such as ocean observation and navigation, this paper presents the design, modeling, fabrication, testing, and analysis of a compact point-absorber wave energy converter (PAWEC) equipped with a mechanical direct-drive power takeoff (PTO) mechanism. The motivation is to address the mismatch between the natural frequencies of conventional PAWECs and dominant ocean wave frequencies, which limits energy capture. The primary objective is to enhance the efficiency of small-scale wave energy converters (WEC) without increasing the buoy size. To achieve this, we introduce a novel design element: an added mass plate (AMP) attached to the buoy. The AMP is devised to increase the WEC added mass and natural period, thereby aligning its natural frequency with dominant ocean wave frequencies. In our case study of a scaled model (1:2.2), the AMP effectively doubled the added mass of the WEC and increased its natural period by 32%. The WEC incorporates a rack and pinion mechanical motion rectifier-type PTO to convert the heave oscillations of the buoy into unidirectional rotation. The scaled model was tested in a wave basin facility with regular waves at zero angle of incidence. The WEC with AMP achieved a maximum root mean square power of 9.34 W, a nearly 30% increase compared to the conventional configuration without AMP, which produced 7.12 W under similar wave conditions. Numerical analysis using the boundary element method in the frequency domain for regular waves confirmed these findings. Finally, it has been derived that the proposed WEC, equipped with an AMP, offers enhanced efficiency in longer wave periods without the need for a larger buoy, establishing its viability as a power source for navigational buoys. This paper also offers a comprehensive guide to experimental techniques for characterizing a PAWEC in a laboratory setting, contributing valuable insights into the wave energy community.

Published under an exclusive license by AIP Publishing. https://doi.org/10.1063/5.0165877

NOMENCLATURE

Abbreviations

OWC

AMadded mass AMPadded mass plate BEMboundary element method CWRcapture width ratio DOF degree of freedom DMDdirect mechanical drive KCKeulegan-Carpenter MMRmechanical motion rectifier

oscillating water column

PAWEC point absorber WEC PTOpower take-off

RAOresponse amplitude operator

RMS root mean square SS stainless steel

WEC wave energy converter

Symbols

added mass (kg)

normalized added mass (m³) added mass coefficient

²Department of Ocean Engineering, Indian Institute of Technology Madras, Chennai 600036, India

a)vishnuvs@umich.edu

^{b)}oe22d012@smail.iitm.ac.in

^{c)}Authors to whom correspondence should be addressed: samad@iitm.ac.in and leizuo@umich.edu

 A_{∞} added mass at infinite frequency (kg) damping coefficient (kg/s) b_d В normalized damping coefficient (m³/rad) В phase lag between \dot{z} and ζ (rad) Csystem damping coefficient (kg/s) hydrodynamic damping coefficient (kg/s) c_{hyd} PTO damping coefficient (kg/s) c_{PTO} F_a amplitude of force (N) damping force (N) F_{damp} diffraction force (N) F_{Diff} F_{ex} excitation force (N) Froude-Krylov force (N) F_{FK} $F_{hyddamp}$ hydrodynamic damping force (N) Mooring force (N) F_m PTO damping force (N) $F_{PTOdamp}$ PTO friction force (N) $F_{PTOfric}$ radiation force (N) F_{rad} hydrostatic restoring force (N) wave height (m) hydrostatic stiffness (N/m) mass of the pinion cage (m) m_{D} mass of standard weights (m) m_s Ν number of peaks Pthe density of water (kg/m³) P_{abs} absorbed power (W) maximum power (W) P_{max} incident wave power (W) P_{wave} r_0, R_0 the radius of the hole (m) R_B the radius of the buoy (m) the radius of the plate (m) R_P Twave period (s) Vthe volume of the fluid (m³) Wcapture width (m) the amplitude of the nth peak (m) x_n initial amplitude (m) heave displacement in the time domain (m) heave amplitude (m) z_a heave velocity (m/s) heave acceleration (m/s²) Δ logarithmic decrement wave elevation (m) damping ratio phase lag between heave force and displacement (rad) φ_z excitation frequency (rad/s) ω damped frequency (rad/s) ω_d natural frequency (rad/s) ω_n

I. INTRODUCTION

Ω

Among renewable energy systems, marine energy systems are getting noticed after the two energy crises in the 1970s and 2000s. Although extensive efforts are going on to harvest wave energy ^{1–5} the system efficiency is still low. Wave energy converter (WEC) devices exhibit diverse designs and functionalities, allowing for varied classification approaches. These classifications can hinge on parameters such as deployment locations, operational principles, modes of operation, and design geometries.⁴ Three primary designs emerge when zeroing

angular frequency (rad/s)

in on the geometric aspect: point absorbers (PAWECs), attenuators, and terminators. Among these wave energy converters (WECs), the PAWECs have a WEC width much less than the wavelength. Distinctly characterized by relatively small dimensions compared to the incident wavelength, PAWECs stand out for their simplicity in the system structure. This inherent simplicity bestows several advantages onto PAWECs: they tend to be easier to manufacture, ensuring reliability in operations and cost-effectiveness during maintenance. Moreover, their compact nature often translates to economic feasibility, making them an appealing choice for small-scale energy harvesting purposes and low-energy seas. Best of the part of t

In the case of a floating PAWEC, a floating body or buoy heaves freely on the ocean surface, which will vibrate with waves. A power takeoff (PTO) mechanism converts the wave energy captured by the buoy into electricity. When a PTO is attached to the buoy, the PTO absorbs energy from the vibration, and then, the buoy amplitude will be reduced. A PAWEC gives maximum power near the resonance zone, where the system's natural frequency matches the wave excitation frequency. As shown by the following equation, the power absorbed by a PAWEC is directly proportional to the displacement of the PTO, which increases with the amplitude of the buoy oscillation:

$$P = \frac{1}{2} c_{PTO} \omega^2 |z|^2, \tag{1}$$

where c_{PTO} is the PTO damping coefficient, ω is the excitation wave frequency, and z is the heave displacement. This means, if the PTO damping coefficient is held constant, to increase the power absorbed, and it is crucial to have the natural frequency of the buoy match the exciting wave frequency to have a large resonant amplitude.

The natural frequency is determined by the hydrostatic stiffness (wet line surface area) and the total mass, including physical and added masses. Usually, small-sized buoys tend to have low natural periods. ¹⁰ The period of an ocean wave is typically 6–15 s, much longer than the natural period of small buoys for ocean observation or marine navigation. Based on Falcao's calculation, ⁴ the diameter of the submerged hemisphere needs to be 52.4 m to match an incident wave frequency of 0.1 Hz, which is too large to be practical. In the literature, many different techniques were used by WEC developers worldwide to match the frequency. For example, two-body wave energy converters have been proposed, which results in a damped natural frequency of the two-body WECs to match the wave frequency in the optimal condition. ¹¹

Similarly, in 2019, Al Shami *et al.* found that the resonant frequency of a WEC can be reduced by increasing its degrees of freedom. Latching control and declutch control were also developed based on this frequency match condition. Heave plates are frequently used in floating offshore structures because they can contribute additional added mass and damping to the system, which improves its hydrodynamic performance. Selfont Also, WECs frequently use submerged heave plates to supply reaction forces between the buoy and the submerged second body. WEC to match its natural frequency with the incoming wave frequency is unexplored. This technique is very different from using a heave plate as a second body in WECs to generate reaction forces, which has been discussed extensively in the literature.

Theoretically, adding a plate to a floating buoy should increase its added mass and reduce its natural frequency in the heave mode. ²³

Based on this reasoning, the performance of a small-size PAWEC in realistic wave periods can be improved by adding a plate called AMP to its buoy. AMPs attached to a float or a buoy in heaving wave motion will have more added mass, which means it will increase the natural period of the system and assist in frequency matching with waves, resulting in higher amplitude. While increasing the added mass and natural period, AMPs ensure that the volume or size of the physical system remains more or less the same. Such a property makes it very useful in the case of small-scale WECs, where a significant amount of capital and operational expenses can be saved by reducing the buoy size. ^{24,25}

WECs can be broadly classified into direct and indirect drives based on the types of PTO systems used. The choice between direct drive and indirect drive PTO significantly impacts the overall design, efficiency, and complexity of the WEC system. A direct-drive WEC uses either a linear or a rotary generator. Direct mechanical drive (DMD) WECs utilize the mechanical energy of wave motion to drive a mechanical generator, like a hydraulic pump, directly. In contrast, direct electrical drive WECs convert wave motion into electricity through a direct coupling with an electric generator, often linear.

While both have merits, for the present PAWEC design, a DMD WEC was chosen due to its ability to effectively handle the high forces and low speeds typical of wave energy, its mechanical simplicity, and potentially higher reliability. A rotary generator was chosen for the current PAWEC over a linear generator due to its higher efficiency, lower cost, and greater availability. Rotary generators are a more mature and widely used technology, benefiting from years of development and refinement, which translates to superior reliability and ease of maintenance in the long run.

Various DMD WEC designs found in the literature exhibit a wide range of characteristics. Certain WECs with Rack and pinion-based PTO mechanisms^{27,28} incorporate a rotary generator coupled with a gearbox. However, these designs lack rectification for the buoy's bidirectional motion. Slider crank-type WECs²⁹ present an alternative but may falter in breaking wave conditions. Winch and rope-type PTO systems³⁰ offer another design path, but these can only harness power during the buoy's upward motion. Mechanical motion rectifier (MMR)-based WECs^{11,31} provide a distinctive solution, employing a unique MMR gearbox to convert the buoy's bidirectional motion into unidirectional rotation, thereby enhancing power generation efficiency. For this reason, a similar MMR-based PTO mechanism is used in the current PAWEC design.

This paper reports the experimental and numerical analysis performed on two different buoy designs (with and without AMP) of a PAWEC equipped with an MMR-based PTO. For both numerical and experimental analyses, the waves considered are linear, regular, and with a zero angle of incidence. A comparative study is done on how various hydrodynamic parameters behave for the two buoy designs. Finally, the results of the analyses were used to adopt the most suitable design that works satisfactorily in real sea conditions. In addition to this, this article contains much information on various experimental methods to characterize a PAWEC, including finding its hydrodynamic parameters, PTO damping, and performance parameters. This information can be beneficial for many wave energy researchers worldwide.

To summarize the significance of this work, this article fundamentally reimagines PAWEC design by introducing the innovative added mass plate (AMP) to the buoy, paving a transformative path for small-scale wave energy conversion. Through rigorous numerical and experimental comparisons against traditional designs, this study underlines the efficacy of the novel AMP-integrated buoy approach. Furthermore, the manuscript meticulously details PAWEC characterization methods elucidate the hydrodynamic advantages of the AMP, and accentuates the cost-effectiveness and compactness of this new design in the realm of small-scale WECs.

The structure of this article is organized as follows. Section II presents the design of the proposed PAWEC system, including the design of individual components like the PTO, the buoy, and the spar. Fundamental concepts regarding the hydrodynamics of WECs are discussed in Sec. III. The numerical modeling of the proposed PAWEC system is presented in Sec. IV. Experimental methods to test the PAWEC are explained in Sec. V. The results of various experiments and numerical simulations are discussed in Sec. VI. Finally, the article is concluded in Sec. VII.

II. DESIGN OVERVIEW

The PAWEC consists of a cylindrical buoy, an AMP connected to the buoy, a spar attached to a bottom fixer plate, and a PTO mechanism [see Fig. 1(c)]. The buoy contains a linear bearing that ensures the spar passes through and reciprocates smoothly. A pair of stands welded on the top surface of the buoy holds the racks (or the PTO mechanism) above water. The mechanism was designed in such a way that it reduces the sealing requirement of the PTO unit. One conventional buoy [Buoy A, Fig. 1(a)] is without an AMP, while the proposed

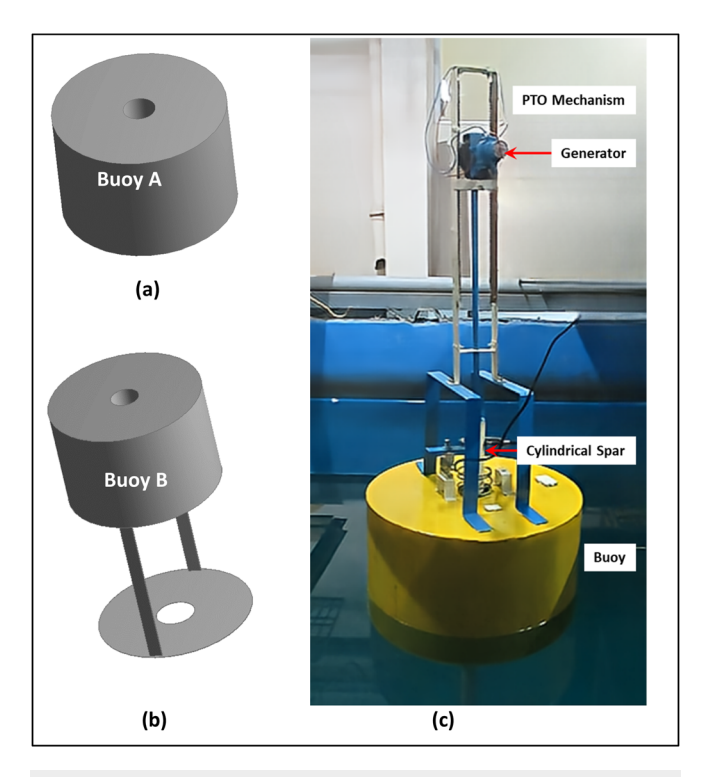


FIG. 1. (a) CAD model of a conventional buoy without AMP (Buoy A). (b) CAD model of the proposed buoy with AMP (Buoy B). (c) Full assembly of the model used for testing in the wave basin.

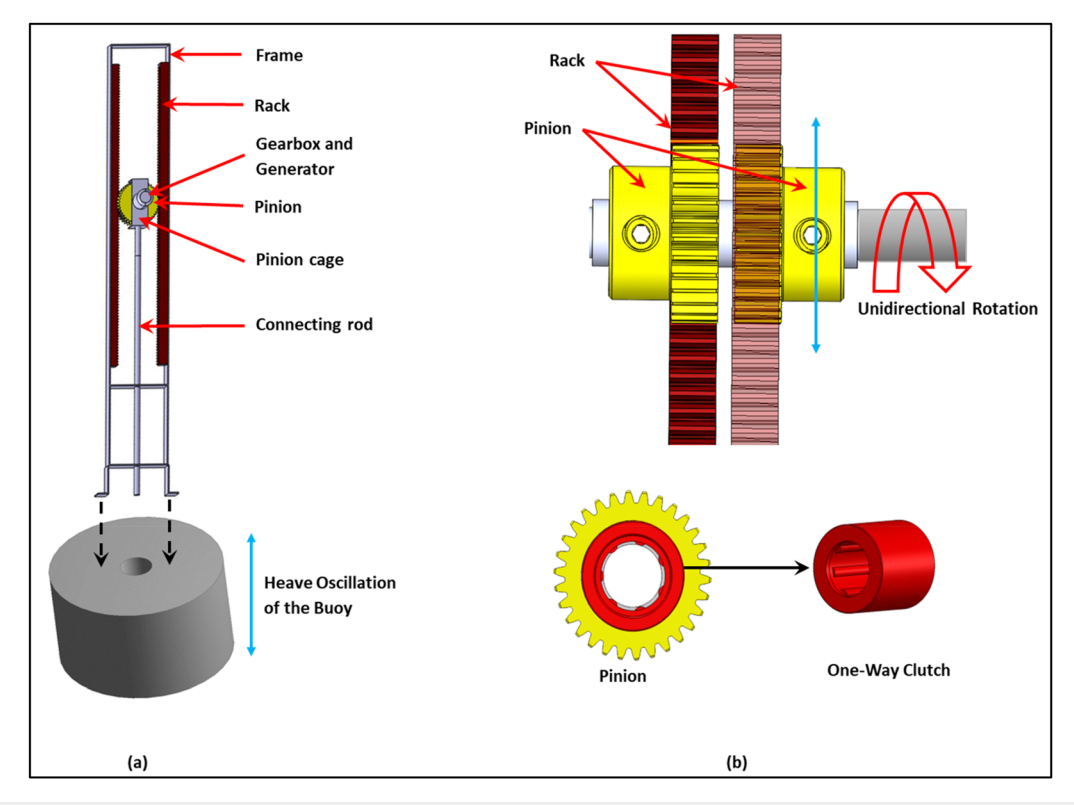


FIG. 2. (a) Design of the power take-off (PTO) mechanism. (b) Pinion with one-way clutch.

buoy connected to an AMP is shown in Fig. 1(b) (Buoy B). The spar is a hollow cylinder that passes through the buoy and supports the PTO unit via the connecting rod. Table I provides the dimensional specifications for the various components of this PAWEC.

When the buoy moves up and down by the action of the waves, the spar slides inside the buoy. The spar is attached to the bottom of the wave basin. Figure 1(c) shows the assembly under testing in the wave basin. The other end of the spar is connected to a pair of pinions mounted on an output shaft connected to a generator. Each pinion engages with one rack and is mounted to the shaft using a one-way clutch to function like a freewheel (Fig. 2). At any given point, only one pair of pinion and rack will drive the output shaft. When the buoy faces the wave crest, it moves up, and a set of the engaged rack and pinion gives shaft rotation in one direction. During wave trough, the other set of the engaged rack and pinion gives shaft rotation in the

TABLE I. WEC component specifications.

Parameter	Value	Units	Parameter	Value	Units
Spar			Bu	oy	
Outer diameter	0.048	m	Diameter	0.6	m
Inner diameter	0.042	m	Height	0.4	m
Thickness	0.003	m	Wall thickness	0.002	m
Length	2	m	Weight	35	kg
Fixer plate	0.1×0.1	m^2	Buoyancy	>50	kg

same direction. Hence, the shaft continuously gets unidirectional motion, which is transferred to the generator to produce electricity. The function of this PTO mechanism is similar to that of the rack and pinion MMR proposed by Liang *et al.*³²

Initially, a CAD was developed based on buoyancy calculations, specifications of the test facility, and ease of fabrication. The four main parts of the design are a buoy, a spar, a fixer plate, and a PTO mechanism. The fabrication material was stainless steel (SAE 316). Figure 3 shows the design flow chart.

The stability analysis was performed frequently during manufacturing to ensure the system's stability.³³ The details of this stability analysis can be seen in Appendix A.

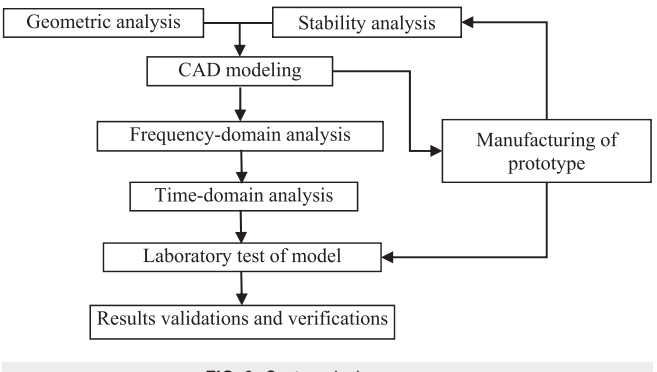


FIG. 3. System design process.

III. HYDRODYNAMICS OF WEC

A. Resonance

A PAWEC absorbs more energy when its natural frequency matches the incoming waves. Usually, the wave period is much longer than the natural period of the WEC vibration. The WEC's natural frequency (ω_n) mainly depends on hydrostatic stiffness (k), buoy radius (R_B) , system mass (m), and added mass (a), 34 shown as follows:

$$\omega_n = \sqrt{\frac{k}{a+m}} = \sqrt{\frac{\rho g \pi R_B^2}{a+m}}.$$
 (2)

However, the boundary element method (BEM) results for different buoy masses showed insignificant change in the natural frequency. The buoy radius and the added mass are the dominant parameters that affect the natural frequency. The WEC was designed to be compact. The WEC's natural frequency was enhanced by adding the AMP.

B. Equation of motion

For simplicity, it was assumed that the WEC has only the heaving motion. The equation of motion of a buoy making a heave displacement z from the mean position is

$$m\ddot{z} = F_{ex} + F_{rad} + F_{res} + F_{hyddamp} + F_{PTO},$$
 (3)

where \ddot{z} , F_{ex} , and F_{rad} are the acceleration of the buoy in the vertical direction, heave excitation force, and wave radiation force, respectively. The hydrostatic restoring force can be calculated as

$$F_{res} = \rho V(t) - mg, \tag{4}$$

where V(t) is an instantaneous draft volume. Assuming linear damping, the hydrodynamic damping is given as

$$F_{hyddamp} = c_{hyd} \dot{z} + \frac{1}{2} c_d \rho A_d \dot{z} |\dot{z}|, \tag{5}$$

where c_{hyd} is the linear hydrodynamic viscous damping coefficient, c_d is the quadratic drag coefficient, and A_d is the characteristic area for drag calculation.

PTO force combines the generator damping, the inertia force, and the mechanical viscous damping

$$F_{PTO} = F_{GenDamp} + F_{Inertia} + F_{PTOfric}.$$
 (6)

The method of experimentally determining PTO force is explained in Sec. V A and Appendix C.

The excitation force (F_{ex}) can be decomposed into two components: the diffraction force (F_{Diff}) caused by wave diffraction and the Froude–Krylov force (F_{FK}) induced by the disturbance in the pressure field due to the presence of a fixed body

$$F_{ex} = F_{Diff} + F_{FK}. (7)$$

Equation (8) shows that the radiation force (F_{rad}) is composed of radiation damping and added mass terms. Added mass is an added inertia during the body's oscillation due to the acceleration of the surrounding fluid. Radiation damping arises when energy is carried away by the waves generated during the oscillation

$$F_{rad} = -[-\omega^2 a(\omega) + j\omega b_d(\omega)]z, \tag{8}$$

where $a(\omega)$ and $b_d(\omega)$ are the frequency-dependent added mass and radiation damping, respectively.

1. Hydrodynamic characterization

Radiation tests determine two significant parameters of any WEC (damping and added mass coefficient) (see Sec. V). The equation of motion for the radiation test is

$$(m + a(\omega)) \ddot{z} + b_d(\omega) \dot{z} + kz = F(t). \tag{9}$$

A load cell measures the excitation force F(t). The relations for the hydrodynamic coefficients³⁵ from Eq. (8) are

$$b_d = +\frac{F_a \sin \varphi_z}{\omega z_a},\tag{10}$$

$$a = -\frac{F_a \cos \varphi_z - kz_a}{\omega^2 z_a} - m,\tag{11}$$

where b_d , a, ϕ_z , F_a , and z_a represent the damping coefficient, added mass, phase lag between excitation and response force, excitation force amplitude, and heave displacement amplitude.

Normalized coefficients can be defined as

$$A(\omega) = \frac{a}{\rho}, \quad A_m = \frac{a}{\rho V}, \quad B(\omega) = \frac{b_d}{\rho \omega},$$
 (12)

where $A(\omega)$ is the normalized added mass, A_m is the normalized added mass coefficient, and $B(\omega)$ is the normalized damping coefficient

2. Concept of added mass plate

Figure 4 shows the concept of increasing the added mass of the buoy by adding a plate to the oscillating buoy. The added mass of a fully submerged circular plate (Fig. 4) is approximately equal to the mass of an imaginary sphere that encloses the plate.¹⁰

The theoretical value of the added mass of a semi-infinite circular cylinder is given by $a = 2.064 \rho r^{3.36}$ From Fig. 4, the approximate theoretical values of added masses a_A and a_B of the buoys without and with AMP, respectively, can be calculated as follows:

$$a_A = \rho \, \pi \left(\frac{2}{3} R_B^3 - r_0^2 R_B \right), \tag{13}$$

$$a_B = \rho \left[\left(\frac{8}{3} R_P^3 - 2\pi R_0^2 R_P \right) + \pi \left(\frac{2}{3} R_B^3 - r_0^2 R_B \right) \right]. \tag{14}$$

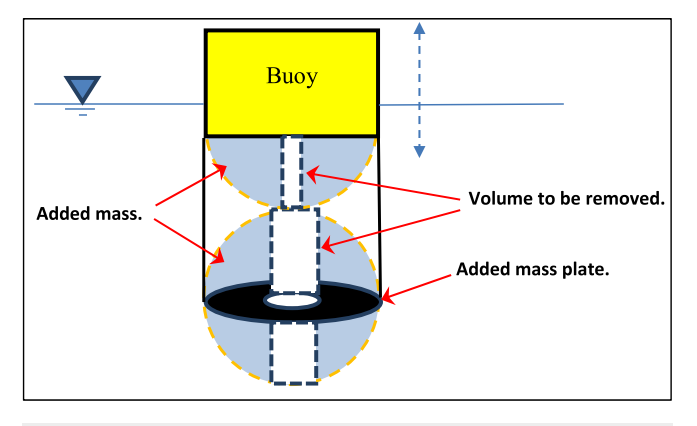


FIG. 4. Calculation of the theoretical added mass of the heaving buoy B.

C. Response amplitude operator (RAO), capture width, and capture width ratio (CWR)

RAO depends on input and output parameters and can be calculated as

$$RAO = \frac{z_a}{n},\tag{15}$$

where z_a is the amplitude of buoy motion, and η is the incoming wave amplitude.

Capture width (W) defined can be calculated as

$$W = \frac{P_{abs}}{P_{wave}}. (16)$$

Sometimes, the absorbed power (P_{abs}) is replaced by the net output power of the WEC in Eq. (16). Incident wave power for regular wave $(P_{wave}, W/m)$ of the crest) can be calculated as

$$P_{wave} = \frac{\rho g^2 T H^2}{32\pi}.\tag{17}$$

For a buoy with diameter D_B of a PAWEC, the capture width ratio (CWR) is expressed as

$$CWR = \frac{W}{D_B}. (18)$$

The maximum possible power absorption for a heaving axisymmetric buoy that radiates ring-shaped waves is given by

$$P_{max} = P_{wave} \left(\lambda / 2\pi \right), \tag{19}$$

where λ is the wavelength.

IV. NUMERICAL MODELING OF THE PAWEC

The code used to model the PAWEC, WEC-Sim, was developed by the Sandia National Laboratory and National Renewable Energy Laboratory and is written in MATLAB/Simulink using the multi-body dynamics solver SimMechanics.³⁷ The code used the Cummins timedomain modeling approach in six degrees of freedom (DOF)³⁸ to formulate the equations of motion for WEC, which is solved for floating body dynamics. The Cummins's equation in the time domain is given as

$$F_{ex}(t) - \int_{-\infty}^{t} f_{rad}(t-\tau) \dot{z}(\tau) d\tau + F_{res}(z) + F_{m}(z,\dot{z})$$
$$+ F_{PTO}(\dot{z}) - F_{hyddamp}(\dot{z}) = (m+A(\infty))\ddot{z}, \tag{20}$$

where the convolution integral is the radiation force, and F_m is the mooring force. Unlike other commercially available time-domain models, developed primarily for naval architecture applications, WEC-Sim is custom-made for WEC applications and was successfully validated by many researchers worldwide. ^{39–41}

The most common methods to model the WECs are frequency domain BEM models, spectral models, and Morrison equation solvers. The selection of an appropriate method depends on the type of work. BEM is often used to derive the hydrodynamic parameters of the bodies, ^{20,42,43} which the time-domain models like WEC-Sim require as an input. BEM solvers solve linear potential theory in the frequency domain and are useful in understanding fundamental hydrodynamics. Even though the time-domain codes are based on the linear

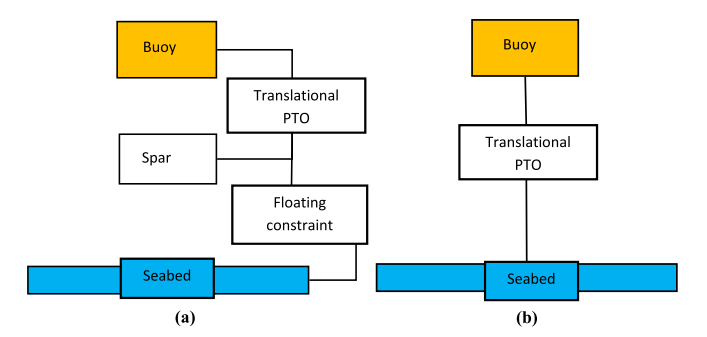


FIG. 5. Simulink models created by WEC-Sim library. (a) Model of the actual design. (b) Model of the experimental model.

hydrodynamic theory, they can also take into account slight nonlinearities. Hence, these models are beneficial in analyzing the performance of WEC.

For this particular PAWEC, AQWA is used as the preprocessor to determine the hydrodynamic parameters. Wall effects can be neglected since the wave basin is equipped with wave absorbers on three of the four sides. Hence, the spatial domain for the analysis is taken as infinite. The depth is the same as that of the wave basin, i.e., 3 m. Since the spar is fixed in the model test, the hydrodynamic analysis is only performed for the buoy. The Simulink model of the actual concept and the labtested model are shown in Figs. 5(a) and 5(b), respectively.

A. Mesh sensitivity study

A grid-independent numerical solution of the system was achieved through different numerical experiments. The meshing information of the three different resolutions for the PAWEC model is reported in Table II. The hydrodynamic coefficients for different meshes are compared in Fig. 6. Figure 6(a) shows that the change in mesh resolution has a negligible effect on the magnitude of the added mass. The relative magnitude of radiation damping tends to decrease by a maximum of 3.9% when the resolution is decreased [Fig. 6(b)]. Although both medium and fine meshes gave almost the same values, considering the computation cost, the medium mesh is chosen for subsequent analysis.

B. Dynamic modeling of the PTO mechanism

 F_{PTO} in Eq. (21) refers to the exciting force acting on the PTO mechanism. This force can be divided into two components, the generator damping force and the inertia force due to the rotational parts [Eq. (6)]. Here, the generator damping force is proportional to the heave velocity, and the inertia force is proportional to the heave acceleration. This gives the equation of motion as

TABLE II. Mesh information.

Туре	Max. element size (m)	Number of elements	Number of nodes
Fine	0.0167	21 034	20 885
Medium	0.0208	14 174	14 316
Coarse	0.025	10 600	10 733

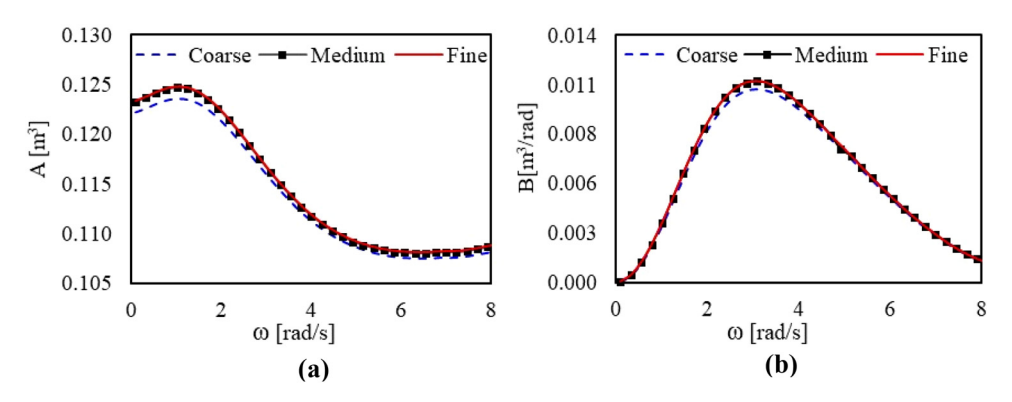


FIG. 6. Mesh dependence; (a) normalized added mass. (b) Normalized radiation damping.

TABLE III. Wave basin specifications.

Parameter	Value	Units	
Length Width	30 30	m m	
Wavemaker type Maximum water depth	Flap 3	m	

$$F_{PTO} = F_{GenDamp} + F_{Inertia} + F_{PTOfric} = c_e \dot{z} + m_e \ddot{z} + F_{PTOfric}. \quad (21)$$

 F_{PTO} given by Eq. (B3) in Appendix B, derived from the above equation of motion, is used to model the PTO mechanism of this PAWEC mathematically. It is worth noting that Eq. (21) is only approximately true when the generator inertia, which is proportional to its mass (m_e) is negligible.

V. EXPERIMENTAL METHODS

Except for the PTO damping test, all other experiments were done in a wave basin (Table III) at IIT Madras, India. A scaling ratio 1:2.2 is adopted based on the Froude scaling law. Specifications of all the instruments used for the experimental measurements are shown in Table IV.

The wave basin's pedals and control unit were periodically calibrated using the MIKE-21 wavefield simulation tool to maintain a certain confidence level in generating specific wave conditions (H and T)

TABLE IV. Instrument specifications.

Instrument	Parameter	Remarks
Accelerometer	Acceleration	Range: ± 5 g pk Sensitivity: 1000 mV/g
Wavemeter/wave gauge	Wave height	Type: Conductive Resolution: <1 mm
Load cell	Load	Capacity: 20 kg
DAQ	Data acquisition	Output: 2.005 mV/V Sample rate: 9600/s Resolution: 16-bit

from the wavemaker. Wave probes continuously monitored the generated wave characteristics during experiments. The sample size and the confidence level of the error band for H and T for regular waves were 30, 95%, ± 0.19 cm, and ± 0.035 s, respectively. As explained before, the two case studies adopted for this study are one buoy without AMP and another similar buoy with an AMP of an outer diameter of 0.6 m, an inner diameter of 0.15 m, and a thickness of 0.002 m connected to its bottom at a distance of 0.6 m. We chose the plate dimensions based on our numerical analysis of various heave plate diameters within the same PAWEC model. 44

A. PTO damping test

The numerical model requires the value of the PTO damping to be entered manually into the code during the analysis. The experiment explained in Appendix C gave the damping values under different load conditions (Fig. 7) that were used for numerical simulations.

B. Determination of hydrodynamic parameters

The hydrodynamic coefficients determined from experiments are compared with those obtained from the BEM results. Since the BEM code does not consider the viscous effects, the value of viscous damping determined experimentally from the free decay and radiation tests

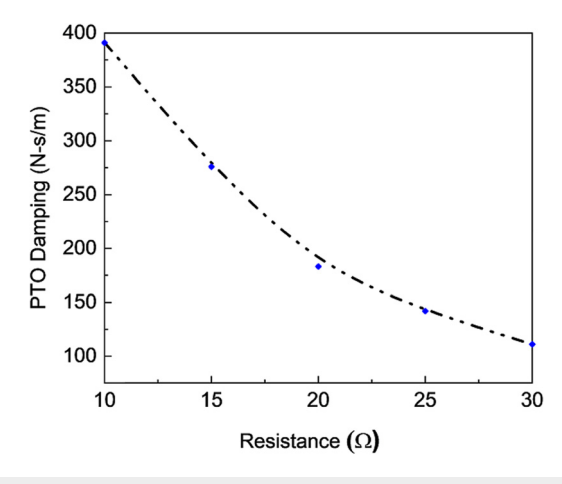


FIG. 7. PTO damping vs load resistance.

is manually added to the code while performing the numerical analysis. In radiation tests, the PAWEC device is forced to oscillate at different frequencies, and the resulting radiation forces are measured. This can provide insight into the frequency-dependent radiation damping of the device. On the other hand, free decay tests involve displacing the WEC device from its equilibrium position and then allowing it to oscillate freely. By observing the decay of these oscillations, we can estimate the total damping (including both radiation and viscous damping) of the WEC system. By comparing the results of these tests to the hydrodynamic coefficients predicted by the BEM analysis, we estimated the additional viscous damping that needs to be included in our WEC-Sim model. Incorporating these experimentally derived viscous damping coefficients into our WEC-Sim model will bolster the precision of our simulations and will align them more closely with real-world WEC performance.

1. Decay tests

A decay test was performed with the model, where the buoy is placed at an initial height from its equilibrium position and is released to go in still water. Now, the buoy's position is measured over time until the buoy comes to rest. The curve obtained will show an exponentially decreasing trend, as shown in Fig. 11, and the system's natural frequency is then determined. From the heave response obtained from the decay test, the natural period and the damping ratio (ξ) for heave motion were computed by using logarithmic decrement (δ), like in the case of an underdamped system⁹ (see Appendix D).

2. Radiation tests

The hydrodynamic coefficients are found by performing radiation tests on the system, as shown in Fig. 8. During the tests, heave

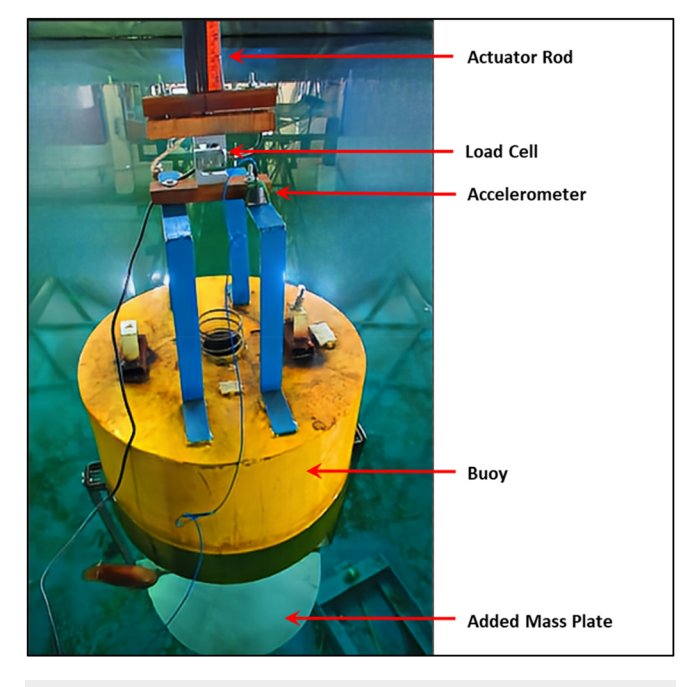


FIG. 8. Radiation test setup installed in the wave basin.

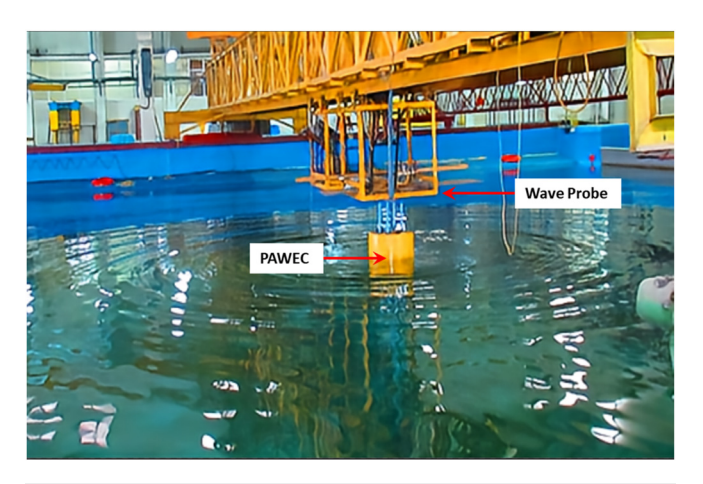


FIG. 9. Radiated wave pattern visible as concentric rings.

motions with varying amplitude and a fixed frequency were applied to the buoy using a linear actuator. The displacement, acceleration, and heave force exerted by the actuator were logged. One wave probe was fixed at a distance of 1 m from the buoy to measure the radiated waves (Fig. 9). The force-time series obtained from the experiment was split into terms of *sines* and *cosines* using Fourier expansion. The force terms for the first harmonics were integrated to find the in-phase and quadrature components. Finally, the radiation and the added mass coefficients were determined from the in-phase and quadrature components using Eqs. (10) and (11), respectively.

C. Diffraction tests

For regular waves ($0.10 \le H \le 0.25 \,\mathrm{m}$ and T = 1, 1.5, 2, and $2.5 \,\mathrm{s}$), wave height, heave displacement, heave force, and power outputs for buoys were measured in a wave basin for regular waves of wave heights ranging from 0.10 to 0.25 m and wave periods 1, 1.5, 2, and 2.5 s. Heave forces were measured by a load cell fixed between the buoy and the clamp once the wave interaction was started (Fig. 10). An accelerometer recorded the buoy acceleration for the incoming waves. The spectral noise density of the accelerometer for the

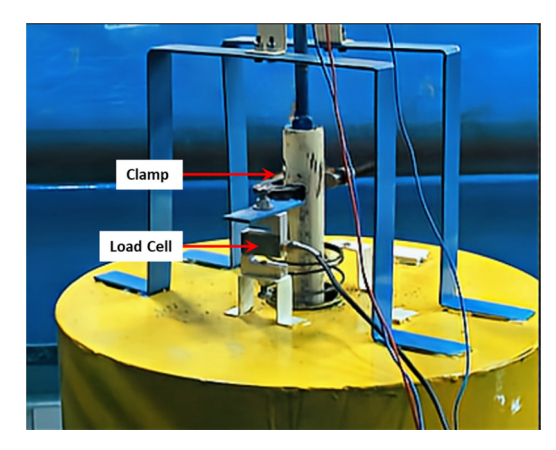


FIG. 10. Load cell to measure the heave forces

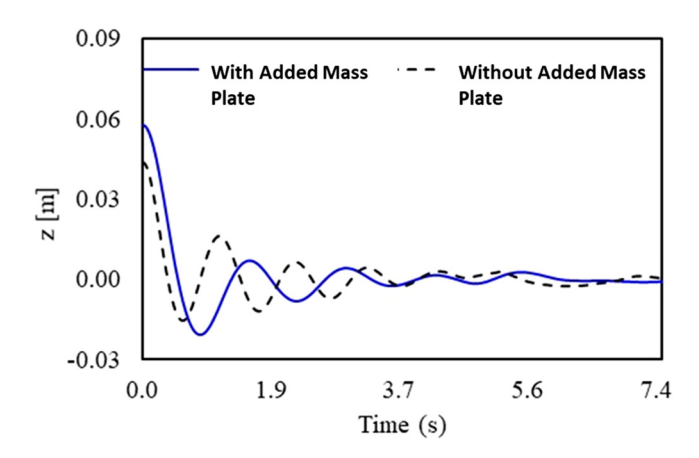


FIG. 11. Time response of free decay tests for buoy A and buoy B.

experiment was about $200 \, \mu g/\sqrt{\text{Hz}}$. At frequency = 0.4 Hz, the double integration error of the data recorded by the accelerometer was \sim 1.5%. There were many practical difficulties that needed to be addressed during the experiments. To maintain the buoy at the fixed location, a fixer plate was fixed at the basin bed instead of a mooring system, as the mooring design was not in the scope of the study. The spar produced frictional loss as lubrication was not allowed in the linear bearings. Minor misalignments during the operation were taken care of by introducing a ball and socket joint between the spar and connecting rod of the PTO. Fixing and recording data from the accelerometer and the load sensor were challenging due to vibrations. Despite these challenges, the desired data were recorded during a small time window, where all systems, including the wave basin, the mechanical and electronic systems, the PAWEC system, and the instruments, worked satisfactorily in tandem.

VI. RESULTS AND DISCUSSION

A. Determination of hydrodynamic coefficients

1. Free decay tests

Free decay tests were performed to determine the damping ratio and the natural period for the heave motion of the buoy. The time history of the buoy movement during decay tests with and without the AMP is shown in Fig. 11. The natural periods of buoy A and buoy B obtained from the BEM code were 1.41 and 1.02 s, respectively. The natural periods of the buoys obtained experimentally and numerically are compared in Table V. The values of other parameters calculated from the free decay experiments using Eqs. (D1)–(D4) are shown in

TABLE V. Heave natural period of the buoy.

	Heave natural period (s)		
Parameters	Experimental	Numerical (BEM)	
Buoy A	1.09	1.02	
Buoy B	1.44	1.41	

Table VI. Inspecting Tables V and VI, one can infer that the AMP increased the system's natural period by \sim 32% while increasing the damping by \sim 37.5%.

2. Radiation tests

Radiation tests are done to determine the normalized radiation damping coefficient and the normalized added mass coefficient of any WEC system. The tests are done for two different amplitudes: 6 and $10\,\mathrm{cm}$, and four different periods: $1.5,\,2,\,2.2,\,\mathrm{and}\,2.5\,\mathrm{s}$. The hydrodynamic coefficients are determined using Eqs. (8)–(14) after substituting the values of required parameters, which have been found experimentally.

a. Radiation coefficient. In terms of normalized radiation damping $[B(\omega)]$, the experimental results show some deviations from the numerically derived values (Fig. 12). This might be due to the reflection of waves from the wave paddle region of the wave basin, where wave absorbers were not present. A similar trend was also observed by Bonfiglio in 2011.⁴⁵ Further analysis of the decay and radiation tests revealed that the radiation damping effect is lower than the total damping, a sum of radiation, and viscous damping. The reason might be that the radiation is a surface phenomenon, and the geometry of the proposed WEC at the surface is small. Also, the radiation damping for the excitation amplitude of 10 cm is slightly higher than that for the amplitude of 6 cm by 6%. This can be explained by the findings of Tao and Cai⁴⁶ that heave damping increases with an increase in the Keulegan- Carpenter (KC) number, which depends on the motion amplitude. Again, as evident in Fig. 12(b), due to the reduced stability of buoy A, more fluctuations occurred during the experiments compared to buoy B. Figure 12 shows that the maximum difference between the numerical and the experimental values occurs near resonance. This could be related to the formation of eddies due to increased buoy velocity near the resonance.

 $b.\ Added\ mass.$ The normalized added mass obtained experimentally and through BEM analysis is shown in Fig. 13. The added mass of buoy B (0.12–0.13 m³ s) is much higher than that of buoy A (0.07–0.05 m³ s). The addition of the AMP increased the added mass of the system significantly because now the system has to displace more fluid when it oscillates. Also, the normalized added mass obtained from BEM analysis and experiments agree

TABLE VI. Values obtained from experimental decay tests.

Parameters	Units	Buoy B	Buoy A
Td	s	1.470	1.100
ω_d	rad/s	4.270	5.710
x_0	m	0.058	0.044
x_n	m	0.004	0.006
δ		1.320	0.960
ξ		0.200	0.150
ω_n	rad/s	4.270	5.780
T_n	s	1.440	1.090

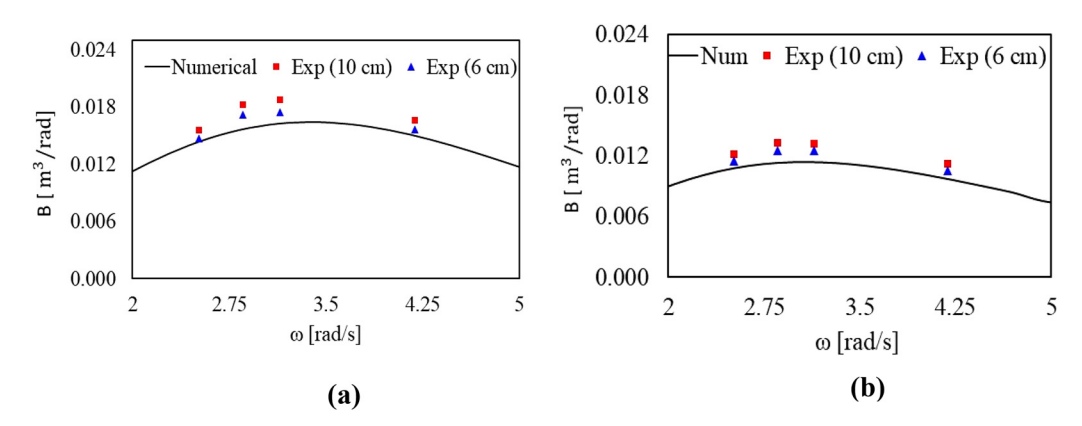


FIG. 12. Normalized radiation damping vs angular frequency. (a) Buoy A. (b) Buoy B.

well within allowable error limits (3%–10%). This may be because the potential theory used in the BEM code also represents the inertial forces.

Although the experimental values for different amplitudes show a small difference with and without AMP, the added mass increased as the oscillation amplitude increased in both cases. The observed variations in the added mass may be attributed to its dependency on the KC number, a behavior it shares with the radiation damping coefficient. However, the KC number in the range of 0.2–1.4 has minimal effect on added mass;⁴⁷ this article does not study the variation of added mass with the KC number.

c. Comparison with theoretical added mass. Based on the theoretical approach mentioned in Sec. III B 2, the added mass of the two different buoy configurations can be calculated from the following equations (13) and (14):

- (i) The theoretical added mass of the buoy $A = \rho \pi (\frac{2}{3} R_B^3) r_0^2 R_B) = 54.64 \text{ kg}.$
- (ii) The theoretical added mass of the buoy $B = \rho \left[\left(\frac{8}{3} R_p^3 2\pi R_0^2 R_p \right) + \pi \left(\frac{2}{3} R_p^3 r_0^2 R_p \right) \right] = 116.01 \text{ kg}.$

Table VII shows the two buoy configurations' theoretical and experimental added mass. The maximum difference (=16.60%) was

seen in buoy B for 2.50 s. This difference might be due to the sudden rise in experimental added mass for a $\omega < 4.5 \, \mathrm{rad/s}$ or a $T > 1.4 \, \mathrm{s}$ [Fig. 13(a)]. The dependence of added mass on the KC number becomes more significant for the KC number outside the range of 0.2–1.2.⁴⁸ Since the resonant frequency of the system of the buoy with AMP lies in the region with $\omega_n < 4.5 \, \text{rad/s}$, velocities in that region will be high, and thus, the values of the KC number will be >1.2. This explains the sudden increase in added mass noticed in Fig. 13. However, the theoretical added mass ignores the effects of the KC number. The difference between the calculated and observed values is more near the resonant region. Similarly, the effect of the KC number on added mass for buoy B increases in the region $\omega < 6 \, \mathrm{rad/s}$ since the system's resonant frequency lies here. Since the rise in added mass for buoy A is more than buoy B, the difference between the calculated value and the observed value of added mass for the former will be more significant (see Table VII).

B. Time domain analysis for monochromatic waves

Time responses of position, velocity, heave force, and power of the buoy configurations were studied experimentally and numerically. Experiments were repeated for wave heights of 0.10, 0.15, and 0.25 m and periods 1, 1.5, 2, and 2.5 s. Due to the constraints imposed by the wave maker's capabilities, achieving the precise resonant periods of the

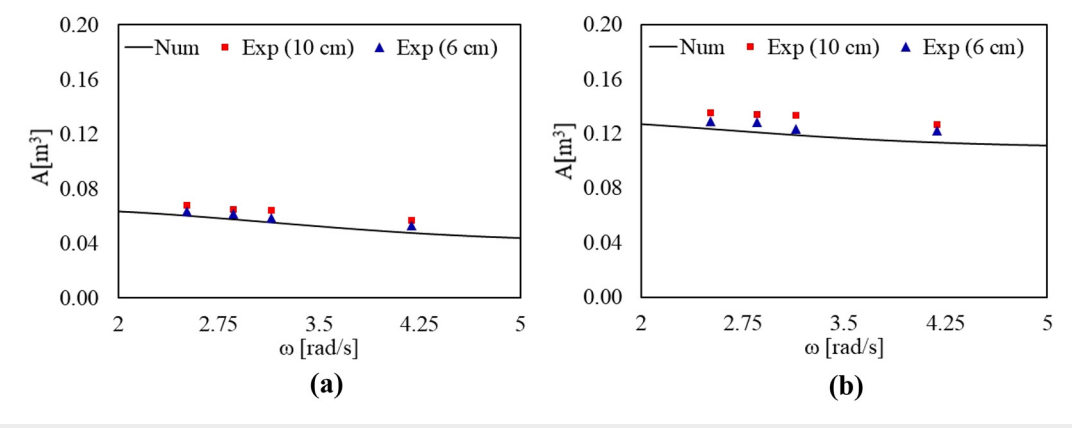


FIG. 13. Normalized added mass vs angular frequency. (a) Buoy A. (b) Buoy B.

TABLE VII. Comparison of heave added mass experimental vs theoretical for the buoy without AMP.

	Buoy	r В	Buoy A		
Period (s)	Experimental added mass (kg)	Difference (%)	Experimental added mass (kg)	Difference (%)	
1.5	126.79	9.30	56.95	4.22	
2.0	133.24	14.86	67.25	23.07	
2.2	134.01	15.52	68.00	24.45	
2.5	135.34	16.60	67.94	24.34	

configurations during the experiment was not feasible. Consequently, periods near the resonance were selected as a practical compromise. The value of PTO damping was found separately through the experiment explained in Sec. V A and was inserted into the WEC-Sim code.

1. Motion response

The amplitude and velocity responses for the heave motion of buoy A and buoy B are shown in Fig. 14. This response is obtained for a regular wave of $H\!=\!0.15$ m and $T\!=\!2.5$ s. The velocity response was obtained experimentally by taking derivatives of displacement recorded by an accelerometer. The experimental values are filtered

using a Butterworth filter with a cutoff frequency of 20 Hz and fitted to a sine curve. In the above-mentioned wave conditions, buoy A and buoy B oscillated with $\omega/\omega_n = 43.50\%$ and 58.90%, respectively. This explains why buoy B shows more displacement than buoy A at this particular period of 2 s. Figure 14 shows that both the buoys are not operating at their resonance; if they were, the phase lag between the wave elevation and velocity (β) of the buoy would have been closer to 0°. If the time difference between the buoy velocity (\dot{z}) and the wave elevation (ζ) is Δ t, then the phase lag (β) can be calculated as

$$\beta = 2\pi \frac{\Delta t}{T}.\tag{22}$$

In 2020, Dafnakis *et al.*⁴⁹ highlighted that the Cummins model overestimates the heave amplitude, attributing this discrepancy to the linear potential theory's overestimation of Froude–Krylov forces or wave excitation loads on submerged buoys. A congruent pattern was noted in our study. The numerical analysis over-predicts the values of heave displacement and velocity by \sim 15%. This may also be due to the frictional losses occurring in moving parts like the rack and pinion or the linear bearing between the buoy and fixed spar. The phase lag β between the wave elevation and buoy velocity also depends on total damping ξ . As ξ is reduced from 0.20 to 0.15 [see Figs. 14(c) and 14(d)], β increased from 81.50° to 85.26°.

a. Linearity test. A linearity test was done to determine the ability of the buoy to be resonant with the incoming wave by examining the

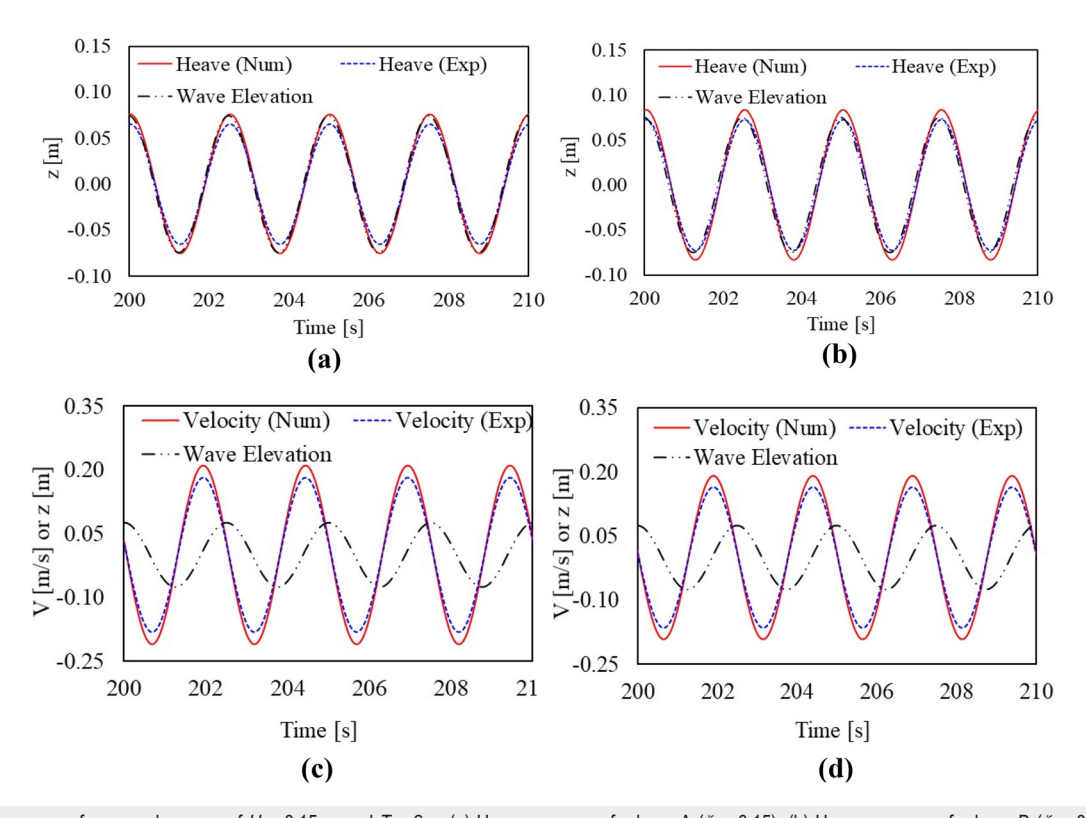


FIG. 14. Motion response for a regular wave of H=0.15 m and T=2 s. (a) Heave response for buoy A ($\xi=0.15$). (b) Heave response for buoy B ($\xi=0.20$). (c) Velocity response for buoy A ($\beta=85.26^{\circ}$).

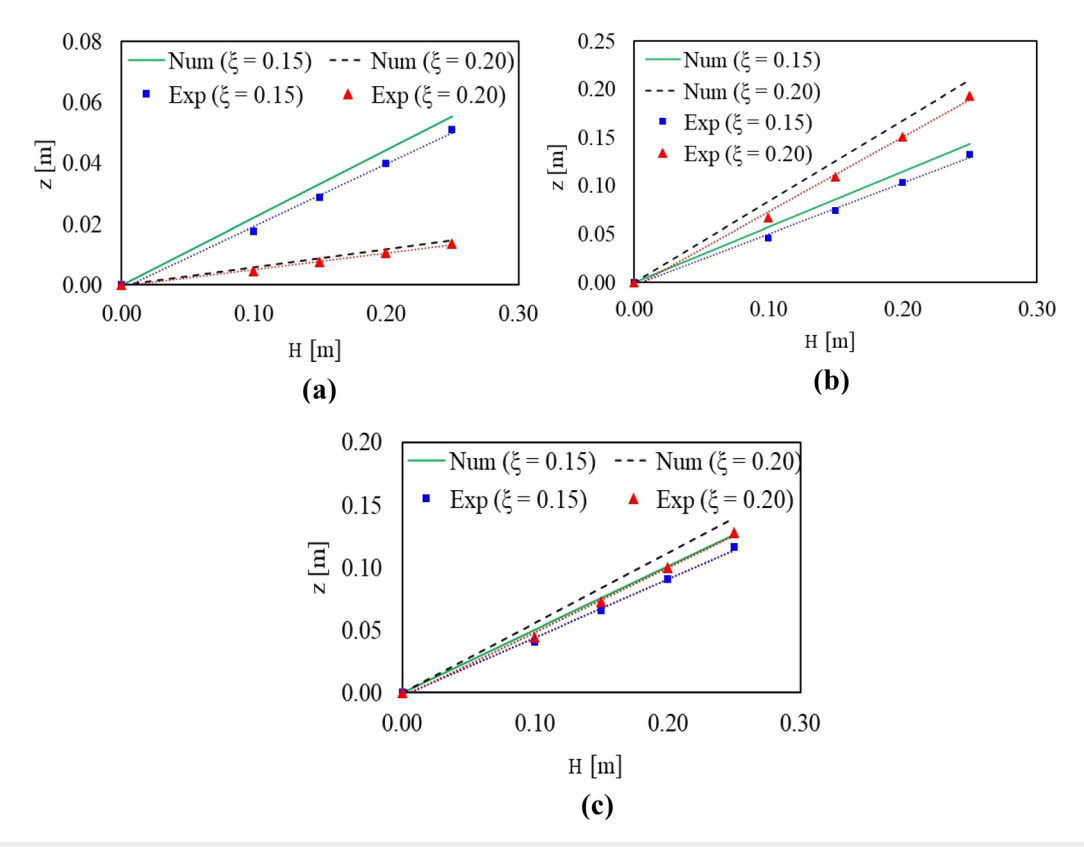


FIG. 15. Linear tests for regular waves with H = 0.10-0.25 m (a) T = 1 s. (b) T = 1.5 s. (c) T = 2.5 s.

variation of the amplitude of the heave motion with the incident wave height. The experimental results were fitted to a straight line passing through the origin. The test was conducted for $H\!=\!0.10$ –0.25 m and $T\!=\!1,1.5$, and 2.5 s. Reasonable linearity is expected when the amplitude of the waves is less than the radius of curvature of the floating body. ^{48,50} The radii of both the buoy configurations are 0.3 m, and the maximum wave height used for testing is 0.25 m. Hence, the condition for linearity is matched; as seen in Fig. 15, the linearity between the heave amplitude and the wave amplitude was good for investigated frequencies.

The values of ω/ω_n for the two different buoy configurations are shown in Table VIII. From Fig. 15, the following observations can be made:

- (i) For T=1 s [Fig. 15(a)], the slope of the line corresponding to buoy A ($\xi=0.15$) is more compared to that of buoy B ($\xi=0.20$). This is because ω/ω_n for buoy A is nearer to resonance at this wave frequency when compared to buoy B. Similarly, for T=1 and 2 s, the slope of the line for buoy B is higher than that for buoy A [Figs. 15(a) and 15(b)].
- (ii) As explained in Sec. VIB1, the difference in the magnitude of heave displacement obtained from numerical and experimental analyses is because of the unaccountability of various factors like friction, generator damping, and non-linearities near the resonant region in the numerical model.

2. Heave excitation force response

The heave excitation forces were measured for both buoys by fixing the buoy while subjecting it to regular waves with varying amplitude and period. Figures 16(a) and 16(b) show the experimental and numerical time response of heave excitation for an incoming wave of $H\!=\!0.15$ m and $T\!=\!1.5$ s. The numerical and experimental values closely match because other unpredictable forces associated with motion will be negligible since the system was fixed during the experiment.

Figures 16(a)–16(c) shows that the excitation force is reduced for a corresponding increase in ξ because of the former's dependence on added mass. The heave excitation force comprises two counteracting components, the diffraction force (F_{Diff}) and the Froude–Krylov force (F_{FK}). For buoy B, the total damping will be higher due to increased added mass. As the added mass increases, the diffraction force component increases for a small change in F_{FK} .

TABLE VIII. $\omega/\omega_{\rm n}$ values for different time periods.

Period (s)	Freq. (rad/s)	ω/ω_n for buoy A	ω/ω_n for buoy B
1.0	6.28	1.09	1.47
1.5	4.19	0.72	0.98
2.5	2.51	0.43	0.59

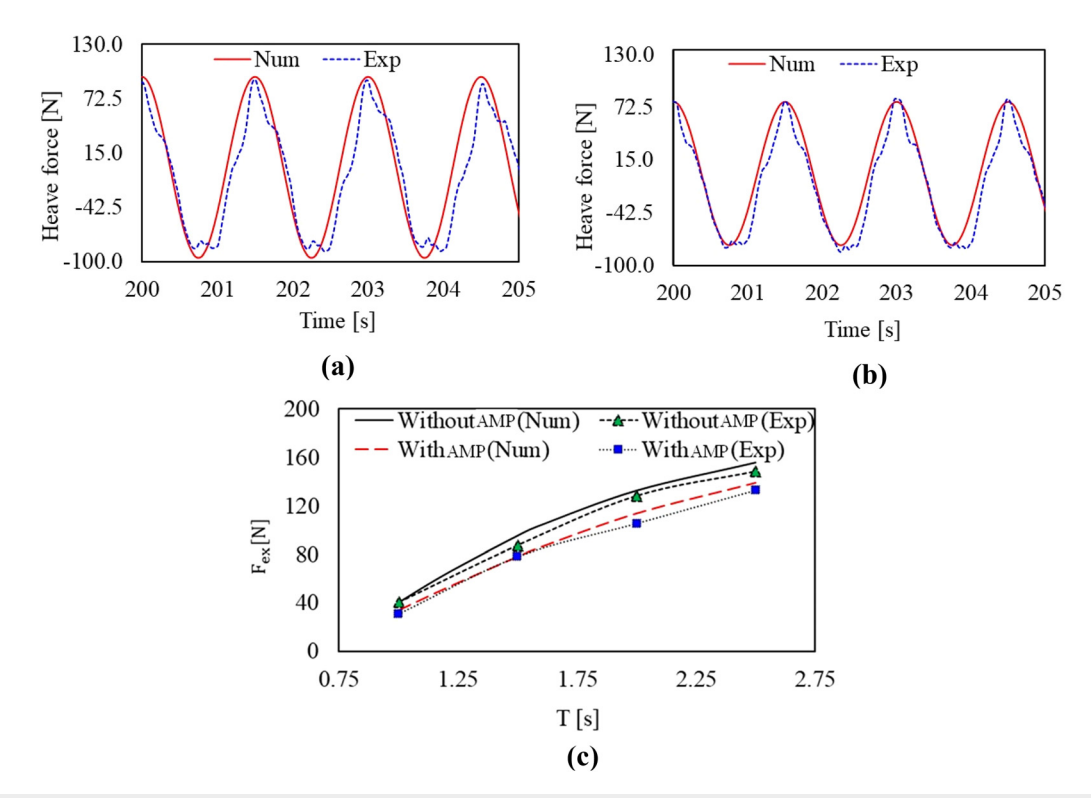
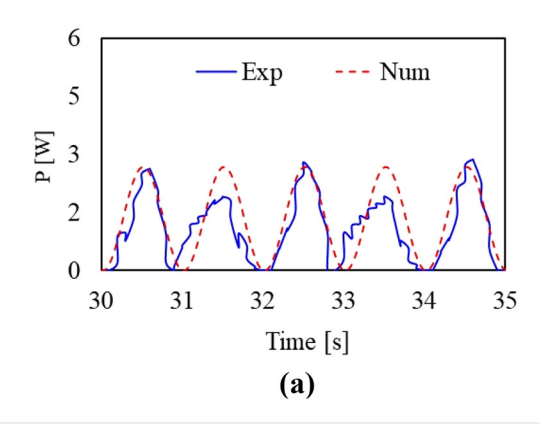


FIG. 16. Heave force measurements for a regular wave of H = 0.15 m. (a) Heave force response for the buoy A ($\xi = 0.15$) at T = 2 s. (b) Heave force response for buoy B ($\xi = 0.20$) at T = 2 s. (c) Variation of excitation force for different wave periods.

Since these two components are 180° out of force, the net heave force derived from potential theory will be the magnitude difference between these two components. Thus, the net heave force reduces as the added mass increases, and this phenomenon is the heave cancelation effect. However, since the dominating component is F_{FK} , this reduction in heave force will be comparatively less and will not significantly affect the power absorption. In Fig. 16(c), for T=1-2.5 s, the maximum reduction of excitation force by adding AMP occurs for 2 s and has a value of 14%.

3. Power response

The hydrodynamic power responses of the buoys obtained for H=0.15 m, T=2 s, and a resistive load of 3 Ω are shown in Fig. 17. A much more refined numerical model of the electric generator is needed to calculate the electric power output more accurately, but that is out of the scope of the present work. Hence, even though Fig. 17 shows a difference of about 19% between the numerically calculated RMS power and the experimentally derived RMS power, most of this



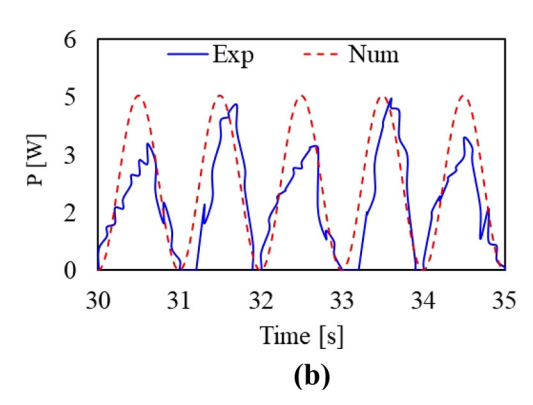


FIG. 17. Power output measurements for a regular wave of H = 0.15 m, T = 2 s. (a) Power response for the buoy A. (b) Power response for buoy B

difference is accounted for by the frictional power loss and the generator damping loss. The frictional loss was significant as the proposed system used a rack and pinion-based PTO mechanism. Figure 17 shows that the pinion's downward stroke gives more power than the upward stroke. This can be due to the assistance of gravity during the downward stroke. However, the numerical model did not predict this phenomenon. From a series of tests with the waves of $T=1-2.5\,\mathrm{s}$, the maximum value of RMS power generated using buoy A and buoy B obtained numerically was 9.48 and 12.34 W, respectively. The same obtained experimentally were 7.12 and 9.19 W, respectively.

C. Performance parameter analysis

As mentioned in Sec. III C, the performance of a WEC is determined by two main parameters, namely, RAO and CWR. Analyses of these parameters can give an idea of the power absorption efficiency of the proposed system.

1. RAO

The buoys and the PTO mechanism were subjected to regular waves with H=0.15~m and T=1-2.5~s. Initially, the RAO increases with T, and after reaching a maximum value, it decreases even if T is increased (Fig. 18). The peak value of RAO for buoy A and buoy B occurred at $T\approx 1.3$ and 1.6~s, respectively. Even though the technical limitations of the wave maker did not allow for generating a wave with a period equal to the numerically derived natural period of the buoys, the numerical values agree well with the experimentally derived values for other periods. Hence, it is safe to assume that these two periods (1.3 and 1.6 s) are the new resonant periods of respective buoys after connecting the PTO mechanism. In other words, adding PTO increased the resonant period of buoy A and buoy B from 1.09 to 1.3 s and 1.43 to 1.6 s, respectively.

In the resonance zone, the linear theory fails to predict the position or power absorption.⁵² Hence, the numerical values are a bit higher than the experimental values near the resonance zone. Payne⁵³ concluded that the difference could be higher for lesser external damping values if viscous damping is ignored during the

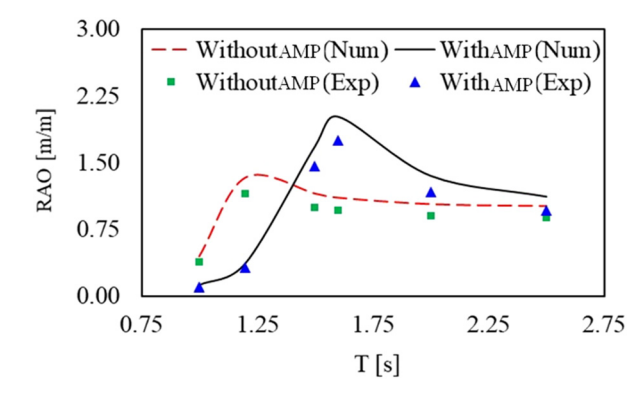


FIG. 18. Response amplitude operators for both the buoy configurations under the action of a regular wave with height, $H\!=\!0.15\,\mathrm{m}$.

numerical analysis. The present work experimentally found the PTO and viscous damping and inserted them into the WEC-Sim code. Therefore, the numerical values near resonance are less compared to other similar works. The peak RAO of buoy B was observed to be higher than that of buoy A. The reason might be that the resonance of buoy B occurs at a higher period than buoy A, and the wave power is higher for a higher period [Eq. (15)].

Buoy A and buoy B performed well for T>1.5 s and T<1.5 s, respectively (Fig. 18). Hence, to improve the performance of the WEC at higher periods, buoy B will be a better option. The numerical model slightly overpredicted the value at resonant peaks because the viscous drag was assumed to be linear in numerical analysis.

2. CWR

CWRs obtained experimentally and numerically for a series of regular waves with H=0.15~m and T=1-2.5~s are shown in Fig. 19. The experimental values were less than the numerical values by about 16.66% at the resonant peaks. A similar phenomenon was observed by So *et al.*⁴¹ They reported that WEC-Sim overpredicted the total energy converted by about 24% for the WEC-CPwr SeaRay. This difference in the present work is a combined effect of three main reasons:

- (i) As mentioned in Sec. VIB3, the power calculated from the experiment is the output power generated by the generator. In contrast, the power calculated by the numerical model is the hydrodynamic power absorbed by the buoy multiplied by the generator efficiency. Thus, the generator loss (beyond 10%) is ignored in the numerical results.
- (ii) As explained in Sec. VIC1, the higher velocity gives higher viscous drag causing the system to behave non-linearly at near-resonant zones. Since the viscous drag is assumed to be linear in the numerical model, it over-predicts the output power.
- The time series of experimental power (Fig. 17) indicates that the peaks produced in the upward and downward strokes are not the same, reducing the RMS value. WECSim code failed to foresee this behavior and, thus, overpredicted the output power.

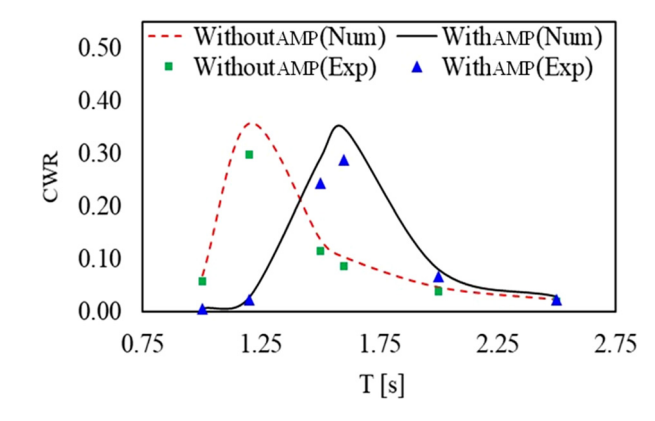


FIG. 19. Capture width ratio for both the buoy configurations under the action of a regular wave with height, H = 0.15 m.

Like RAO, the CWR increases with the period and peaks at $T \approx 1.2$ and 1.6 s for buoy A and buoy B, respectively (Fig. 19). The CWR for buoy B is higher for T < 1.6 than buoy A. The peak CWR of buoy B is 3% less than that of buoy A. The AMP in buoy B increases the system's damping and reduces the conversion efficiency. Even though a small percentage reduces the peak, the curve obtained for buoy B is wider than that obtained for buoy A. This means buoy B is more efficient for a wider range of frequencies than the other buoy configuration. This is desirable in real sea conditions where the frequencies of sea waves lie over a wider range.

VII. CONCLUSION

This paper proposed and validated using an added mass plate (AMP) to tune the natural frequency of a point absorber-type wave energy converter (PAWEC) to match the exciting wave frequency for small power applications. A 1:2.2 scaled version of an innovative PAWEC was prototyped, numerically analyzed, and tested in the wave tank. The paper also details the experimental characterization of a PAWEC, which can benefit many readers working in wave energy. The main conclusions drawn are as follows:

- (i) The AMP attached to the buoy increases the added mass by a factor of ~2.16 and the natural period of the system by ~32.10% without increasing the size of the WEC.
- (ii) The PAWEC with AMP (Buoy B) performed well for longperiod waves, while the buoy without AMP (Buoy A) performed well for short-period waves.
- (iii) The numerical model predicted the heave response of both the buoy configurations well except at the resonance, where it overpredicted the position by a maximum of 15%.
- (iv) The numerical model estimated the power absorbed with a peak over prediction of 16.66% near the resonance.

Considering the disadvantages of modeling a system operating in its resonance region using linear approximations, the overprediction of results by the numerical model is justifiable. Further works are being carried out to replace the fixed central tube with a floating spar and study the WEC response in irregular waves.

ACKNOWLEDGMENTS

V. Vijayasankar, S. Kumar, and A. Samad thank the financial support from the IP cell, IIT Madras (Project ID: ICS/16–17/831/RR1E/MAHS). V. Vijayasankar and L. Zuo wish to thank the support from U.S. NSF IUCRC No. 1738689.

AUTHOR DECLARATIONS Conflict of Interest

The authors have no conflicts to disclose.

Author Contributions

Vishnu Vijayasankar: Conceptualization (equal); Data curation (equal); Formal analysis (equal); Methodology (equal); Visualization (equal); Writing – original draft (equal); Writing – review & editing (equal). Suman Kumar: Conceptualization (supporting); Data curation (equal); Methodology (supporting); Visualization (equal); Writing – original draft (supporting); Writing – review & editing (supporting).

Abdus Samad: Conceptualization (equal); Methodology (equal); Resources (equal); Supervision (equal); Writing – original draft (equal); Writing – review & editing (equal). Lei Zuo: Conceptualization (equal); Funding acquisition (equal); Resources (equal); Supervision (equal); Writing – original draft (equal); Writing – review & editing (equal).

DATA AVAILABILITY

The data that support the findings of this study are available from the corresponding authors upon reasonable request.

APPENDIX A: STABILITY ANALYSIS

The optimized stability parameters of the buoy obtained after multiple design iterations are listed in Table IX. A floating buoy is stable when the metacenter is above the center of gravity.³³ The metacentric radius is given by

$$BM = \frac{I}{V},\tag{A1}$$

where I is the second moment of inertia of the water plane area, and V is the displaced volume of water. In Fig. 20, M, G, and B stand for the metacenter, the center of gravity, and the center of buoyancy, respectively. In other words, the buoy is stable if the metacentric height is positive (GM > 0).

In the full-scale design, the floating spar will have a drag plate instead of fixing it to the seabed and will be moored. The large surface area of a drag plate gives a large drag and creates a relative motion between the spar and the buoy. In that case, stability

TABLE IX. Stability parameters.

Parameter	Value	Units	
Metacentric radius (BM) GB	0.09	m m	
GM	0.02	m	

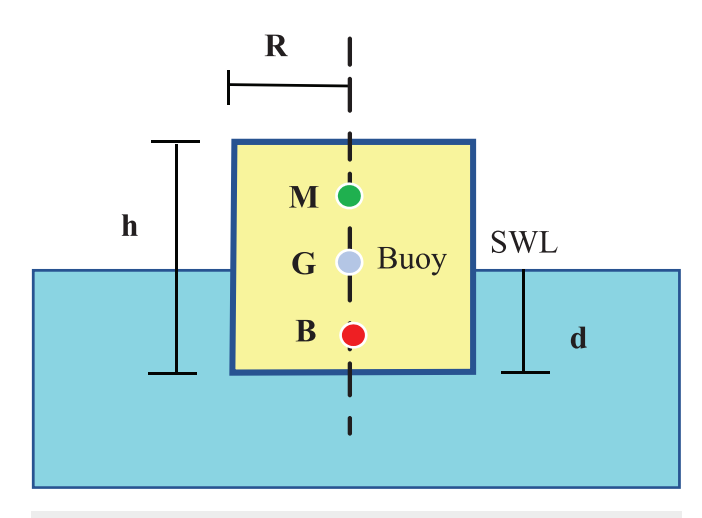


FIG. 20. Preliminary stability parameters.

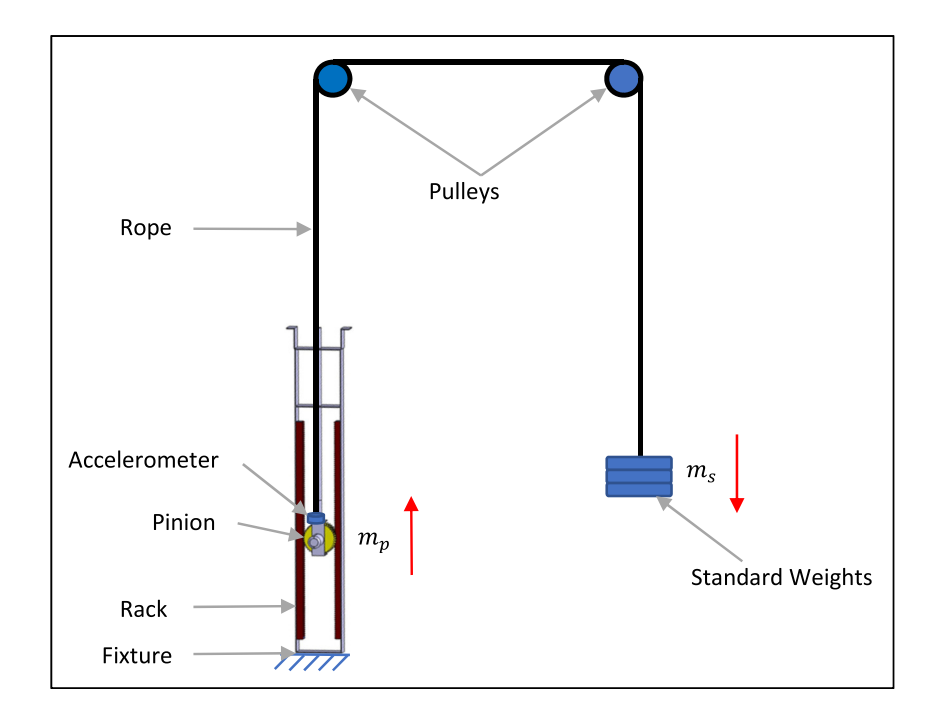


FIG. 21. Test setup for measuring the PTO friction and damping.

analysis should be performed for the spar and the buoy. The spar in the present case was fixed to the wave basin floor because of the basin depth limitation (=3 m).

APPENDIX B: DERIVATION OF EQUATION FOR THE PTO FORCE

Assuming k_t and k_e are the torque and speed constants of the generator, respectively, and R_i and R_o are the internal resistance and the load resistance, the expression for equivalent generator damping can be obtained as

$$c_e = \frac{k_t k_e n^2}{(R_i + R_o) r^2},$$
 (B1)

where n is the gearbox gear ratio, and r is the radius of the pinion.

Now, the equivalent mass is the sum of the mass of the oscillating rack and the inertial mass of all the rotating components

$$m_e = 2m_r + \frac{2J_p + J_c + J_s + J_{gb} + n^2 J_{ge}}{r^2},$$
 (B2)

where m_r is the mass of the rack, and J_p , J_c , J_s , J_{gb} , J_{ge} are the moment of inertia of the pinion, one-way clutch, shaft, gearbox, and generator, respectively.

Substituting (B1) and (B2) in (21), the equation of motion can be derived as

$$F_{PTO} = 2m_r + \left(\frac{2J_p + J_c + J_s + J_{gb} + n^2 J_{ge}}{r^2}\right) \ddot{Z} + \left(\frac{k_t k_e n^2}{(R_i + R_o) r^2}\right) \dot{Z}.$$
(B3)

APPENDIX C: EXPERIMENT TO DETERMINE PTO DAMPING

An experiment determines this damping (see Fig. 21), wherein the pinion cage was accelerated by dropping standard weights tied to a rope passing over two low-friction pulleys. An accelerometer connected to the cage records its acceleration. The equation of motion of such a setup can be written as

$$(m_s - m_p)g - c_e \dot{z} - F_{PTOfric} = m_p \ddot{z}, \tag{C1}$$

where $F_{PTOfric}$ is the friction between the rack and pinion, whose value was found at different load conditions. m_s and m_p are the masses of standard weights and the pinion, respectively.

APPENDIX D: EQUATIONS FOR DECAY TESTS

The expressions used for finding the natural frequency of an undamped oscillation are

$$\delta = \frac{1}{n} \ln \left(\frac{x_0}{x_n} \right),\tag{D1}$$

$$\xi = \frac{1}{\sqrt{1 + \left(\frac{2\pi}{\delta}\right)^2}}.$$
 (D2)

Damped natural frequency, ω_d , can be formulated as

$$\omega_d = \frac{2\pi}{T_d},\tag{D3}$$

where the damped period, T_d , can be obtained from the dynamic free response of the PAWEC.

Undamped natural frequency, ω_n , is expressed as

$$\omega_n = \frac{\omega_d}{\sqrt{1 - \xi^2}}.$$
(D4)

REFERENCES

- ¹T. K. Das, K. Kumar, and A. Samad, "Experimental analysis of a biplane wells turbine under different load conditions," Energy **206**, 118205 (2020).
- ²P. Halder, H. Takebe, K. Pawitan, J. Fujita, S. Misumi, and T. Shintake, "Turbine characteristics of wave energy conversion device for extraction power using breaking waves," Energies 13, 966 (2020).
- ³S. Ravikumar, R. Anandanarayanan, A. George, B. Pattanaik, P. V. Dudhgaonkar, P. Jalihal *et al.*, "Experimental investigation of a bidirectional impulse turbine for oscillating flows at various resistive loads," IEEE J. Oceanic Eng. 46, 115–131 (2021).
- ⁴A. F. d. O. Falcão, "Wave energy utilization: A review of the technologies," Renewable Sustainable Energy Rev. 14, 899–918 (2010).
- ⁵T. Aderinto and H. Li, "Ocean Wave energy converters: Status and challenges," Energies 11, 1250 (2018).
- ⁶B. Guo and J. V. Ringwood, "Geometric optimisation of wave energy conversion devices: A survey," Appl. Energy 297, 117100 (2021).
- ⁷K. Budar and J. Falnes, "A resonant point absorber of ocean-wave power," Nature 256, 478–479 (1975).
- ⁸S. Foteinis, "Wave energy converters in low energy seas: Current state and opportunities," Renewable Sustainable Energy Rev. **162**, 112448 (2022).
- ⁹A. Pecher, "Handbook of ocean wave energy," *Ocean Engineering and Oceanography* (Springer, 2017), Vol. 7.
- 10 T. Sarpkaya, Wave Forces on Offstructure Structures, 1st ed. (Cambridge University Press, 2010).
- ¹¹C. Liang and L. Zuo, "On the dynamics and design of a two-body wave energy converter," Renewable Energy 101, 265–274 (2017).
- ¹²E. Al Shami, X. Wang, and X. Ji, "A study of the effects of increasing the degrees of freedom of a point-absorber wave energy converter on its harvesting performance," Mech. Syst. Signal Process. 133, 106281 (2019).
- performance," Mech. Syst. Signal Process. 133, 106281 (2019).

 13 A. Babarit and A. H. Clément, "Optimal latching control of a wave energy device in regular and irregular waves," Appl. Ocean Res. 28, 77–91 (2006).
- ¹⁴A. Babarit, M. Guglielmi, and A. H. Clément, "Declutching control of a wave energy converter," Ocean Eng. 36, 1015–1024 (2009).
- ¹⁵M. Lake and A. W. Troesch, "Hydrodynamic coefficient estimation for TLP and spar structures," J. Offshore Mech. Arct. Eng. 122, 118–124 (2000).
- ¹⁶R. Antonutti, C. Peyrard, L. Johanning, A. Incecik, and D. Ingram, "An investigation of the effects of wind-induced inclination on floating wind turbine dynamics: Heave plate excursion," Ocean Eng. 91, 208–217 (2014).
- ¹⁷L. Tao and D. Dray, "Hydrodynamic performance of solid and porous heave plates," Ocean Eng. 35, 1006–1014 (2008).
- ¹⁸J. Li, S. Liu, M. Zhao, and B. Teng, "Experimental investigation of the hydrodynamic characteristics of heave plates using forced oscillation," Ocean Eng. 66, 82–91 (2013).
- ¹⁹A. Brown, J. Thomson, and C. Rusch, "Hydrodynamic coefficients of heave plates, with application to wave energy conversion," IEEE J. Oceanic Eng. 43, 983–996 (2018).
- ²⁰S. J. Beatty, M. Hall, B. J. Buckham, P. Wild, and B. Bocking, "Experimental and numerical comparisons of self-reacting point absorber wave energy converters in regular waves," Ocean Eng. 104, 370–386 (2015).
- ²¹X. Li, C. Liang, C. A. Chen, Q. Xiong, R. G. Parker, and L. Zuo, "Optimum power analysis of a self-reactive wave energy point absorber with mechanically-driven power take-offs," Energy 195, 116927 (2020).
- ²²S. Chen, B. Jiang, X. Li, J. Huang, X. Wu, Q. Xiong et al., "Design, dynamic modeling and wave basin verification of a hybrid wave-current energy converter," Appl. Energy 321, 119320 (2022).
- ²³L. Tao and S. Cai, "Heave motion suppression of a spar with a heave plate," Ocean Eng. 31, 669–692 (2004).
- ²⁴A. de Andres, R. Guanche, C. Vidal, and I. J. Losada, "Adaptability of a generic wave energy converter to different climate conditions," Renewable Energy 78, 322–333 (2015).

- ²⁵A. de Andres, J. Maillet, J. H. Todalshaug, P. Möller, D. Bould, and H. Jeffrey, "Techno-economic related metrics for a wave energy converters feasibility assessment," Sustainability 8, 1109 (2016).
- ²⁶N. J. Baker and M. A. Mueller, "Direct drive wave energy converters," Rev. Energies Renouvelables 4, 1–7 (2001), p..
- ²⁷P. Rosa-santos and F. Taveira-pinto, "CECO wave energy converter: Experimental proof of concept," J. Renewable Sustainable Energy 7, 061704 (2015).
- 28S. Chandrasekaran and H. Sinhmar, "Power generation using mechanical wave energy converter," Int. J. Ocean Clim. Syst. 3, 57–70 (2012).
- 29H. B. Karayaka, H. Mahlke, D. Bogucki, M. Mehrubeoglu, A. Texas, and M. U. Christi, "A rotational wave energy conversion system development and validation with real ocean wave data," in *Proceedings of the IEEE Power and Energy Society General Meeting* (IEEE, 2011), pp. 5–11.
- 30]. Sjolte, G. Tjensvoll, and M. Molinas, "Power collection from wave energy farms," Appl. Sci. 3, 420-436 (2013).
- ³¹X. Li, C. A. Chen, Q. Li, L. Xu, C. Liang, K. Ngo et al., "A compact mechanical power take-off for wave energy converters: Design, analysis, and test verification," Appl. Energy 278, 115459 (2020).
- ³²C. Liang, J. Ai, and L. Zuo, "Design, fabrication, simulation and testing of an ocean wave energy converter with mechanical motion rectifier," Ocean Eng. 136, 190–200 (2017).
- ³³M. Faizal, M. R. Ahmed, and Y. H. Lee, "A design outline for floating point absorber wave energy converters," Adv. Mech. Eng. 6, 846097 (2014).
- 34 M. Eriksson, J. Isberg, and M. Leijon, "Hydrodynamic modelling of a direct drive wave energy converter," Int. J. Eng. Sci. 43, 1377–1387 (2005).
- 35 J. H. Vugts, "The hydrodynamic coefficients for swaying, heaving and rolling cylinders," Int. Shipbuild. Prog. 15, 251–275 (1968).
- 36J. N. Newman, Marine Hydrodynamics, 40th anniversary ed. (The MIT Press, London, 2005).
- ³⁷K. Ruehl, D. Ogden, Y.-H. Yu, A. Keester, N. Tom, D. Forbush, J. Leon, J. Grasberger, and S. Husain, WEC-Sim, Version v5.0.1 (2022).
- ³⁸R. So, S. Casey, S. Kanner, A. Simmons, and T. K. A. Brekken, "PTO-Sim: Development of a power take off modeling tool for ocean wave energy conversion," in *Proceedings of the IEEE Power and Energy Society General Meeting* (IEEE, 2015), pp. 1–5.
- ³⁹K. Ruehl, C. Michelen, S. Kanner, M. Lawson, and Y. H. Yu, "Preliminary verification and validation of WEC-Sim, an open-source wave energy converter design tool," in *Proceedings of the ASME 33rd International Conference on Ocean, Offshore and Arctic Engineering* (ASME, San Francisco, CA, 2014).
- ⁴⁰Y. Yu, K. Hallett, L. Ye, and C. Hotimsky, "Design and analysis for a floating oscillating surge wave energy converter," in *Proceedings of the ASME 2014 33rd International Conference on Ocean, Offshore and Arctic Engineering*, San Francisco, CA, 2014 (ASME, New York, NY, 2014), pp. 1–10.
- ⁴¹R. So, S. Member, C. Michelen, B. Bosma, P. Lenee-bluhm, T. K. A. Brekken et al., "Statistical analysis of a 1:7 scale field test wave energy converter using WEC-Sim," IEEE Trans. Sustainable Energy 8, 1118–1126 (2017).
- ⁴²G. Backer, Hydrodynamic Design Optimization of Wave Energy Converters Consisting of Heaving Point Absorbers (Ghent University, Belgium, 2009), pp. 1–3.
- ⁴³J. Pastor and Y. Liu, "Frequency and time domain modeling and power output for a heaving point absorber wave energy converter," Int. J. Energy Environ. Eng. 5, 101 (2014).
- 44V. Vijayasankar and A. Samad, "Analyzing different methods to increase the natural period of a compact wave energy converter," *Trends in Manufacturing* and Engineering Management, Lecture Notes in Mechanical Engineering (Springer Science and Business Media, Deutschland GmbH, 2021), pp. 901, 1001
- ⁴⁵L. Bonfiglio, "Added mass and damping of oscillating bodies: A fully viscous numerical approach," in *Recent Advances in Fluid Mechanics, Heat & Mass Transfer and Biology*, Vol. 1 (WSEAS Press, Puerto Morelos, Mexico, 2011), pp. 210–215.
- 46¹L. Tao and S. Cai, "Heave motion suppression of a spar with a heave plate," Ocean Eng. 31, 669–692 (2004).
- ⁴⁷L. Zhu and H. Lim, "Hydrodynamic characteristics of a separated heave plate mounted at a vertical circular cylinder," Ocean Eng. 131, 213–223 (2017).
- 48Z. Zang, Q. Zhang, Y. Qi, and X. Fu, "Hydrodynamic responses and efficiency analyses of a heaving-buoy wave energy converter with PTO damping in regular and irregular waves," Renewable Energy 116, 527–542 (2018).

- 49 P. Dafnakis, A. P. S. Bhalla, S. A. Sirigu, M. Bonfanti, G. Bracco, and G. Mattiazzo, "Comparison of wave-structure interaction dynamics of a submerged cylindrical point absorber with three degrees of freedom using potential flow and computational fluid dynamics models," Phys. Fluids 32, 093307 (2020).
- 50 T. Bjarte-Larsson, M. Lillbekken per, J. Hals, and J. Falnes, "Model experiment on an OWC type wave energy converter with hydraulic power take-off," in Proceedings of the OMAE 21st International Conference on Offshore Mechanics and Arctic Engineering (ASME, Oslo, Norway, 2002).
- ⁵¹A. Haslum, Simplified Methods Applied to Nonlinear Motion of Spar Platforms
- (Norwegian University of Science and Technology, 2000).

 52M. Durand, A. Babarit, B. Pettinotti, O. Quillard, J. L. Toularastel, and A. H. Clément, "Experimental validation of the performances of the SEAREV wave energy converter with real time latching control," in Proceedings of the 7th European Wave and Tidal Energy Conference (2007).
- 53G. S. Payne, Numerical Modelling of a Sloped Wave Energy Device (The University of Edinburgh, 2006).